REVIEW

Converting Molecular Vibration to Mechanical Wave for Bond-Selective Imaging of Deep Tissue†

Jie Hui[a], Ji-xin Cheng[b,c*]

a. Department of Physics and Astronomy, Purdue University, West Lafayette, Indiana 47907, USA
b. Weldon School of Biomedical Engineering, Purdue University, West Lafayette, Indiana 47907, USA
c. Department of Chemistry, Purdue University, West Lafayette, Indiana 47907, USA

(Dated: Received on April 4, 2015; Accepted on April 27, 2015)

As an emerging label-free imaging modality with chemical selectivity and millimeter-depth resolvability, vibrational photoacoustic imaging provides a new avenue to map chemical content in biological tissue. It heralds the potential for detection of white matter loss and regeneration, assessment of breast tumor margin, and clinical diagnosis of vulnerable plaques in atherosclerosis. In this work, we provide an overview of the development of bond-selective photoacoustic imaging and various biomedical applications enabled by this new technology.

Key words: Label-free, Vibrational spectroscopy, Chemical imaging

I. INTRODUCTION

Enabling the detection of specific molecules within cells and tissues, molecular vibration is the basis of numerous microscopy approaches. Among these are Raman scattering and infrared absorption vibrational microscopies, which have been widely used for chemical imaging in biomedicine [1]. Similarly, such nonlinear vibrational methods as coherent anti-Stokes Raman scattering (CARS) and stimulated Raman scattering (SRS) microscopy have enabled new discoveries in biomedical imaging, thanks to high sensitivity and 3D spatial resolution [2−4]. But, because all these approaches are limited to an imaging depth of a few hundred micrometers in biological tissue, their potential use in clinical settings is restricted.

A deep-tissue imaging approach able to maintain high chemical selectivity and spatial resolution would certainly satisfy diagnostic needs in biomedicine. A promising solution is a photoacoustic (PA) platform combining light illumination with acoustic detection based on the PA effect discovered by Bell as early as 1880 [5]. The PA signal can be generated by either microwave or pulsed laser. In PA imaging, a pulsed laser beam illuminates a specimen, which contains optical absorbers with significant absorption at the laser wavelength. After much scattering in tissue, the diffused photons are delivered to and absorbed by the target molecules. Part of the optical energy is converted to heat in the region of the absorbers, which results in a local temperature rise on the order of millikelvins and the subsequent generation of acoustic waves. The acoustic waves then can be recorded by an ultrasound transducer in real time. The time-of-flight of the PA signal contains information of the locations of the absorbers, so the distribution of the absorbers can be reconstructed from the measured signal (Fig.1).

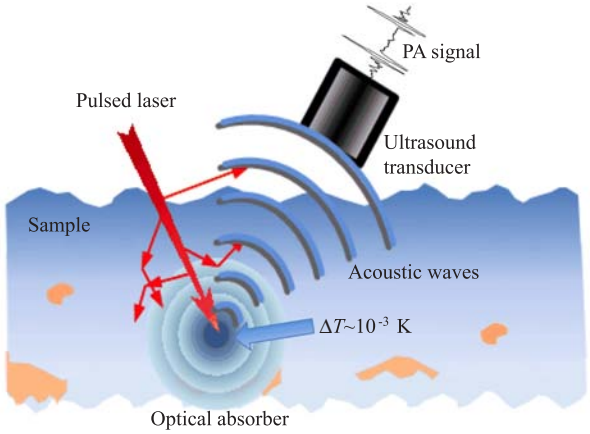

FIG. 1 Schematic of PA signal generation and detection.

The PA imaging technique offers several unique advantages over its pure optical counterparts. First, it can achieve higher resolution in deep tissue based on the detection of acoustic waves, as the acoustic scattering in tissue is one thousand-fold weaker than the optical scattering. Second, because the PA signal originates from the absorption of photons, it eliminates the background caused by scattering and offers a molecular contrast based on optical absorption. Third, the generation of PA signal does not depend solely on ballistic photons; diffused photons equally contribute to the sig-

†Dedicated to Professor Qing-shi Zhu on the occasion of his 70th birthday.
*Author to whom correspondence should be addressed. E-mail: jcheng@purdue.edu, Tel.: +1-765-4944335, FAX: +1-765-4961912

nal, which leads to a centimeter-scale imaging depth in a tomography configuration.

Harnessing these advantages, researchers have developed various PA imaging platforms, including photoacoustic microscopy (PAM), photoacoustic tomography (PAT), and intravascular photoacoustic imaging (IVPA). Wang and Hu described the various PA imaging approaches in a comprehensive review [6]. Besides PA imaging of hemoglobin, exogenous PA contrast agents such as dyes and nanoparticles have been intensively investigated over the years [7, 8].

II. NEW CONTRAST MECHANISM

In 2007, our laboratory performed a theoretical study to explain our unexpected observation of Raman-resonance induced photodamage in CARS imaging [9]. We found that with tight focusing, about 0.01% of the excitation energy is transferred to the specimen via the SRS process that occurs simultaneously with CARS. Because molecular absorption could produce an ultrasound signal for deep-tissue imaging, as shown in photoacoustic detection of hemoglobin by others [6], we began to explore whether we could "hear" the SRS with a transducer. We spent two years, but no ultrasound signal was detected under the tissue photodamage threshold.

Although frustrated, we decided to try once more by using aqueous carbon disulfide (CS_2), a molecule known to produce a strong signal of Raman-induced Kerr effect. We scanned the optical parametric oscillator (OPO) idler wavelength to search for the Raman-stimulated PA signal and found a strong ultrasound spike at 850 nm for the OPO and 1064 nm for the YAG. Surprisingly, the wavenumber difference of the two excitation beams did not match with any Raman band of CS_2. Moreover, the signal remained when the YAG laser was blocked. We immediately realized that we were observing a completely new process that is likely based on overtone excitation of CS_2 vibration. This finding led to our development of vibrational photoacoustic (VPA) microscopy [10]. Using the second overtone of the C−H bond, we demonstrated 3D VPA imaging of lipid-rich atherosclerotic plaques by excitation from the artery lumen.

According to the anharmonicity theory, the transition frequency for an overtone band has the following relation with the fundamental frequency,

$$\nu = \nu_0 n - \chi\nu_0(n + n^2) \tag{1}$$

where ν_0 is the transition frequency of fundamental vibration, χ is the anharmonicity constant, and n=2, 3, $\cdots$, represents the first, second, and subsequent overtones [11]. When the frequency of incident laser light matches the transition frequency of overtone, the energy of the incident photons is absorbed and then induces a local rise in temperature (Fig.2). The accumulated

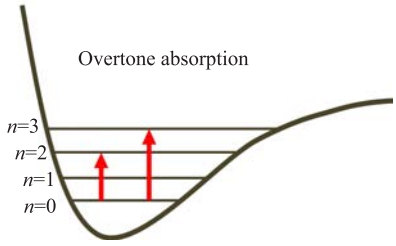

FIG. 2 Schematic of first and second overtone absorption of a molecule.

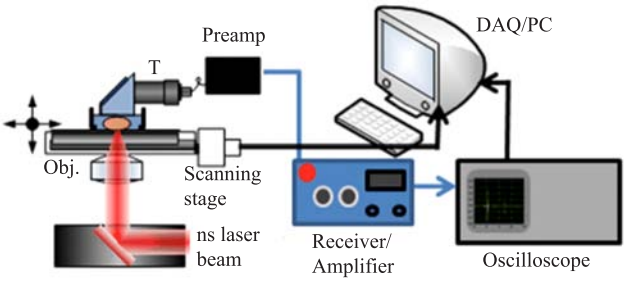

FIG. 3 Vibration-based photoacoustic imaging on an inverted microscope incorporates an ultrasound transducer (T) and a red nanosecond laser beam [10].

heat is then released through thermal-elastic expansion in tissue, which generates mechanical vibrations in the form of acoustic waves [10].

In our first vibration-based PA imaging modality, the illumination was generated by a 5 ns Nd:YAG pumped OPO laser system (Fig.3) [10]. A doublet lens was used to weakly focus the beam, which simultaneously provides sufficient spatial resolution and energy density for VPA signal generation. A focused transducer, preamplifier, and signal receiver then collected and processed the signal. We customized an ultrasound coupler using a water-glass interface to redirect signal to the transducer. Such a configuration separates the transducer from laser radiation to protect it from radiation-induced heat and noise. The envelope of the VPA signal amplitude was recorded for further analysis and image reconstruction. The 3D VPA imaging can be performed by integrating an XY translational stage into the system for sample scanning.

Given that O−H and C−H are the most abundant chemical bonds in biological tissues, it is promising to develop bond-selective VPA imaging modalities for visualization of water with abundant O−H bonds, and lipid bodies and protein aggregate with correlating abundant CH_2 and CH_3 groups, respectively. Based on the microscopy imaging system, a VPA spectroscopic study of biologically significant samples was conducted to determine the suitable wavelengths for VPA imaging of these specimens (Fig.4) [10, 12].

Electronic absorption of hemoglobin is dominant in an optical window ranging from the visible to the NIR region between 400 nm and 1.0 μm (Fig.4(a)).

DOI:10.1063/1674-0068/28/cjcp1504069

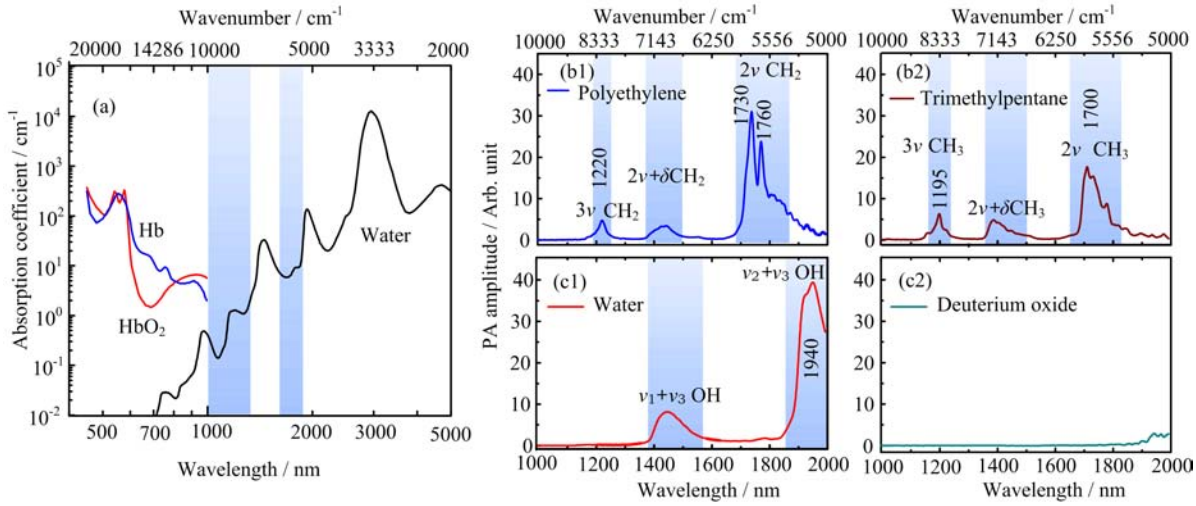

FIG. 4 PA spectra of various chemical bond vibrations: (a) whole blood and pure water, (b) polyethylene and trimethylpentane, and (c) water and deuterium oxide [12].

Hemoglobin absorption overwhelms the third- and higher-order C−H overtone transitions located in the same region. For wavelengths longer than 1.0 μm, significant water absorption due to overtone transitions of O−H bonds reduces the penetration of the photons in the specimens. Nevertheless, two optical windows exist in the water vibrational absorption spectrum, 1000−1300 and 1600−1850 nm (highlighted in light blue). Importantly, the second and first overtone transitions of C−H bond are located in the same windows. These spectral features produce two optical windows for C−H bond-selective imaging [12].

Wang *et al.* in our laboratory performed a detailed analysis of VPA spectra of C−H, O−H, and O−D bonds [12]. As shown in Fig.4(b), polyethylene provides the absorption profile of the methylene group (CH_2), for which the first overtone (2ν CH_2) shows two primary peaks at around 1730 nm (5800 cm^{-1}) and 1760 nm (5680 cm^{-1}). The stronger peak at 1730 nm is generally thought to be a combination band of asymmetric and symmetric stretching. The 1760 nm peak is assigned to the first overtone of stretching. The second combination band of CH_2, located between 1350 and 1500 nm, is attributed to the combination of harmonic stretching and a non-stretching mode, such as bending, twisting, and rocking $2\nu+\delta$. The second overtone of CH_2 stretching is peaked at around 1210 nm. It is shown that the PA amplitude at 1730 nm is around 6.3 times of that at 1210 nm. The spectrum of trimethylpentane is mainly contributed by the absorption profile of methyl groups (CH_3). The primary peak at around 1700 nm (5880 cm^{-1}) is assigned to the first overtone of CH_3 stretching.

It is clear that the CH_2 and CH_3 groups have distinguishable profiles at the first overtone region. The second combination band of CH_3 starts from 1350 nm to 1500 nm, with the main peak at around 1380 nm, which is generally thought to be $2\nu+\delta$. The second overtone of CH_3 stretching shows the primary peak at around 1195 nm. Figure 4(c) shows the VPA spectra of H_2O and D_2O liquid in the 1.0−2.0 μm window. The $\nu_2+\nu_3$ combinational band and the $\nu_1+\nu_3$ combinational band appear at 1940 and 1450 nm, respectively. Here, ν_1, ν_2, and ν_3 denote the symmetric, bending, and asymmetric vibrations of the water molecule, respectively. Due to the heavier mass of deuterium, the prominent overtone and combinational bands of D_2O are located at longer wavelengths. Thus, D_2O can be used as an acoustic coupling agent during vibration-based PA imaging.

III. MAPPING LIPID-LADEN PLAQUES

Lipid deposition is a major hallmark of atherosclerosis, and one that determines lesion progression and plaque vulnerability to rupture. Accurate characterization of the lipid content in an arterial wall would enable a phenomenal improvement for vascular intervention in diagnosis and treatment of atherosclerosis. Over the last few years, many research groups put efforts to find the suitable wavelengths for PA imaging of atherosclerotic plaques [10, 12−14].

Wang *et al.* performed 3D label-free VPA imaging of lipid-rich atherosclerotic plaques of carotid arteries in the optical window of 1000 nm to 1300 nm [10]. The arteries were harvested from Ossabaw pigs having metabolic syndrome and profound atherosclerosis. The imaging configuration is shown in Fig.5(a) with optical excitation from the lumen side of the artery. VPA spectroscopy at different sites of atherosclerotic arterial walls has demonstrated clearly the capability of imaging different levels of lipid deposition inside arterial walls (Fig.5(b)). Locations I−III correspond to a thickened intima, an intermediate plaque without a

DOI:10.1063/1674-0068/28/cjcp1504069

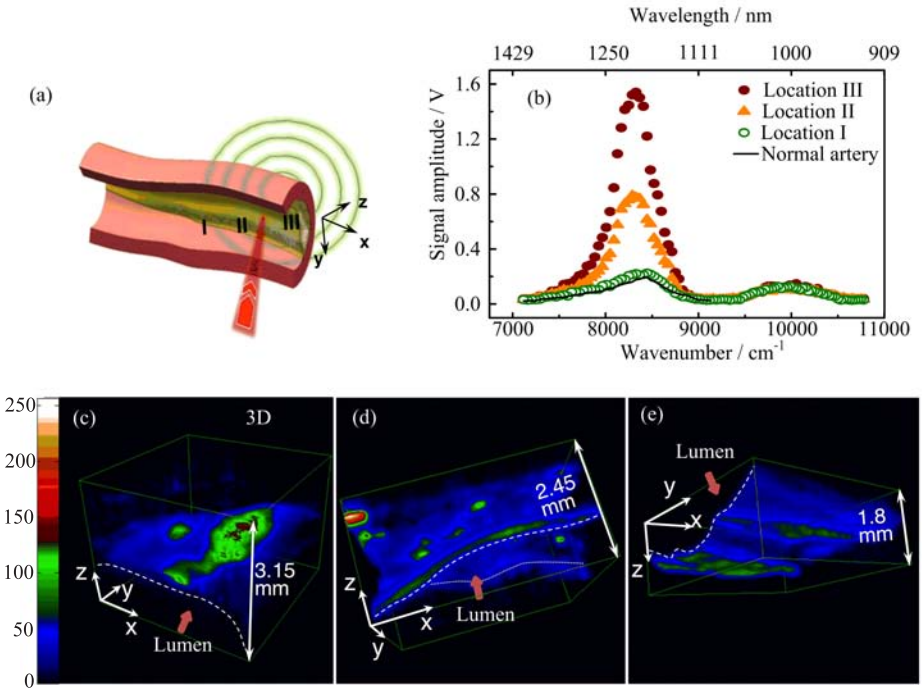

FIG. 5 Lipid mapping of an atherosclerotic artery by VPA microscopy. (a) Schematic of luminal inspection of an atherosclerotic artery by VPA microscopy, (b) VPA spectra elucidating progressively greater levels of lipid deposition inside an arterial wall at locations I, II, and III compared to a normal artery with no lipid deposition, (c) 3D-reconstructed VPA images of a confluent lipid core in an atherosclerotic artery, (d) scattered lipid deposition in an arterial wall, and (e) mild fatty streaks [10].

necrotic core or fibrotic lesion, and a relatively advanced lesion with the formation of a lipid core, respectively. According to the VPA spectra of the lipid depositions, they used an excitation laser at 1195 nm for 3D VPA imaging of atherosclerotic lipid deposition for optimal vibrational contrast. Their images elucidate the spectra of the different milieus of lipid accumulation in the arterial wall, such as a confluent lipid core in an atherosclerotic artery, a scattered lipid deposition in an arterial wall, and the formation of mild fatty streaks in early atheroma (Fig.5 (c)−(e)). A strong VPA signal from lipids located at 1.5 mm can be detected below the lumen.

Beyond lab-based microscopy studies of lipid-laden plaques in an atherosclerotic artery, intravascular photoacoustic (IVPA) imaging has recently been developed to image lipid-laden atherosclerotic plaque by multiple groups [15−20]. It has been considered as a promising technique for quantifying the amount of lipid deposition, a key indicator of plaque vulnerability, in the arterial wall. However, the imaging systems still suffer from slow imaging speed due to the lack of suitable laser source to excite the molecular overtone vibration at high repetition rate.

Wang *et al.* recently demonstrated a 2-kHz master oscillator power amplifier (MOPA)-pumped, barium nitrite ($Ba(NO_3)_2$) Raman laser, which improved the IVPA imaging speed by two orders of magnitude, to 1.0 s per frame [18]. In the laser system, a 1064 nm pulsed laser at a repetition rate of 2-kHz generated by the MOPA laser was used to pump the $Ba(NO_3)_2$-based Raman shifter (Fig.6). Through stimulated Raman scattering process, the 1064 nm pump laser is converted to a 1197 nm output, which matches the second overtone vibration of C−H bond and thus can be used to excite the lipid-rich plaques for PA imaging.

By the laser system, Wang *et al.* further demonstrated the high-speed IVPA imaging of an iliac artery from an Ossabaw pig model with atherosclerosis (Fig.7) [18]. The cross-sectional IVPA (Fig.7(a)), intravascular ultrasound (IVUS) (Fig.7(b)), and the merged (Fig.7(c)) images of the atherosclerotic artery clearly show the complementary information of the artery wall. Importantly, lipid deposition on the arterial wall, which is not seen in the IVUS image, shows clear contrast in the IVPA image. This result has been further validated by the histology of the same artery (Fig.7(d)). The white area in the histology image from hematoxylin and eosin (H&E) staining shows the location of the lipid deposition. For both IVPA and IVUS imaging, 2000 A-lines were acquired for the cross-sectional image, resulting in a 1 Hz frame rate. This laser system enabled the high-speed IVPA imaging of lipid-laden plaque, which is nearly two orders of magnitude faster than the previously reported systems [16, 17, 19].

DOI:10.1063/1674-0068/28/cjcp1504069

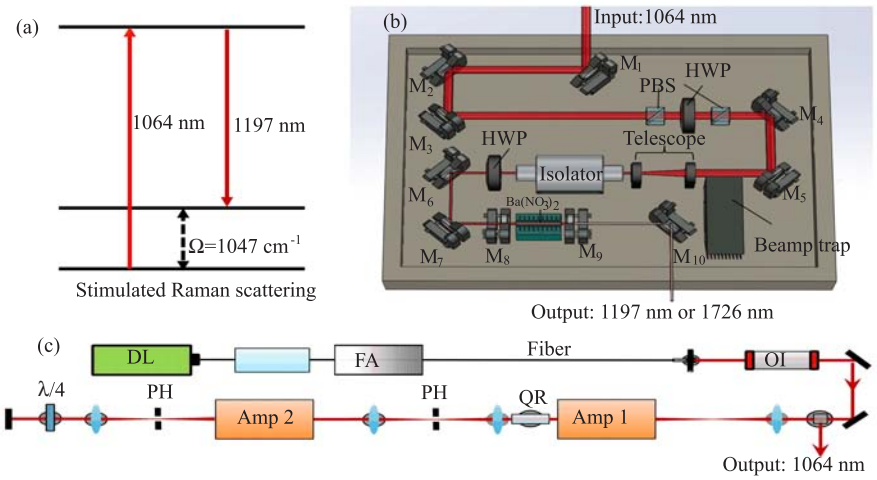

FIG. 6 Principles and schematics of the Raman laser system. (a) the principle of the $Ba(NO_3)_2$ crystal-based Raman shifter, (b) the schematic of the Raman shifter where M_1-M_7: 45-degree 1064 nm reflective mirror, PBS: polarizing beam splitter, HWP: half wave plate, M_8: resonator end mirror, M_9: output coupler, M_{10}: silver mirror, (c) the schematic of the MOPA system where Amp: amplifier, PH: pin hole, QR: quartz rotator, OI: optical isolator, FA: fiber amplifier, DL: directly modulated diode laser [18].

IV. ASSESSING WHITE MATTER LOSS AND REGENERATION

VPA imaging is also a valuable label-free imaging tool for assessing the progression of white matter pathology after spinal cord injury in a rat model as well as the treatment effects of neuroprotective therapeutics.

As reported by Wu *et al.*, VPA spectroscopy was performed to determine its ability to characterize the histology of a normal rat spinal cord and to search the optimal wavelength for VPA imaging of the white matter as shown in Fig.8(a) [21]. The CH_2-rich white matter has two peaks, one located at 1730 nm and the other at 1200 nm, corresponding to the first and second overtones of CH_3 vibration, respectively. C-scan VPA imaging of cross-sectional slices of a rat spinal cord was performed to check the contrast difference between white and grey matters at 1730 nm excitation, which is likely caused by higher CH_2 density in white matter (Fig.8(b)). B-scan VPA imaging of fixed intact spinal cord at 1730 nm excitation was also performed as shown in Fig.8(c). A 200 μm penetration depth for white matter and 1.3 mm at the dorsolateral surface of the cord above the dorsal horn were observed. The higher scattering coefficient of white matter (296 cm^{-1} at 1064 nm) over gray matter (57 cm^{-1} at 1064 nm) explains the penetration difference. These results have suggested that the high VPA contrast and high scattering coefficient represent a unique feature of white matter in VPA images, allowing us to examine white matter morphology and changes in the normal and injured spinal cords.

Wu *et al.* compared VPA images showing normal and injured spinal cords to determine whether VPA is a sensitive measure of pathological changes (Fig.8 (d) and (e)). Further, they evaluated a neuroprotective treatment with ferulic acid conjugated glycol chitosan (FA-GC) to determine whether VPA imaging is sensitive for assessing the neuroprotective effect of a treatment agent (Fig.8(f)). In the B-scan VPA cross-section image of the injured spinal cord, the dorsal portion of the cord shows two times lower VPA signal than that of the normal spinal cord, indicating a lower CH_2 density.

Histology with Luxol fast blue staining (Fig.8

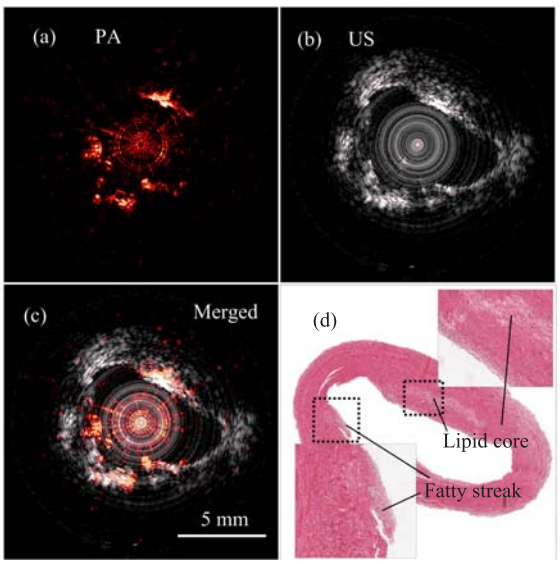

FIG. 7 High-speed imaging of an atherosclerotic artery. (a) IVPA, (b) IVUS, and (c) merged IVPA/IVUS image; (d) histology of the artery cross-section of the area imaged by IVPA method. The 5 mm spatial calibration applies to all panels [18].

DOI:10.1063/1674-0068/28/cjcp1504069

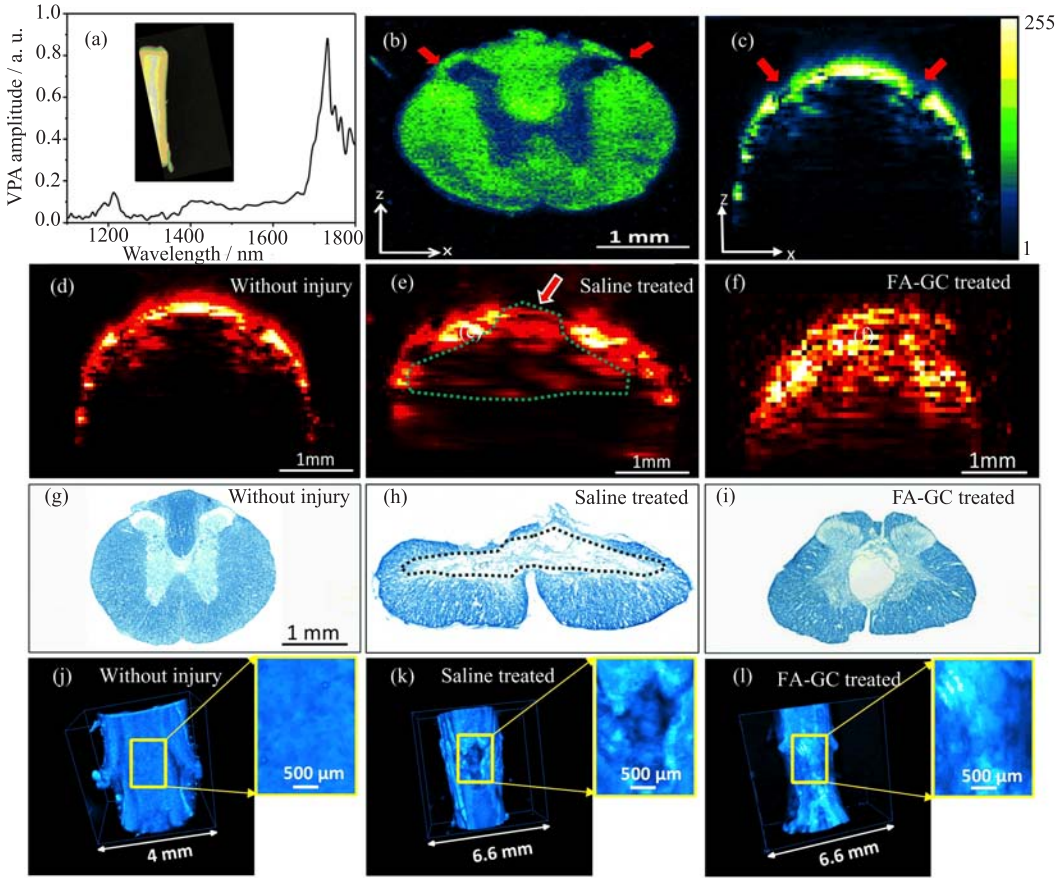

FIG. 8 VPA spectra and comparison of spinal cord with/without contusive injury harvested at day 28 post-injury. (a) VPA spectra of white matter of spinal cord, (b) VPA image of cross-sectioned normal spinal cord, (c) B-scan of whole spinal cord without injury, (d)−(f) B-scan VPA image of normal spinal cord tissue, and of contusive injured tissue with or without treatment, (g)−(i) Luxol fast blue staining of myelin in normal spinal cord, and in contusive injured spinal cord with or without treatment, and (j)−(l) 3D PA image showing the white matter loss in normal spinal cord, and in injured spinal cord with and without treatment. Insets show the enlarged images of the spinal cord, dashed lines indicate white matter loss [21]. The arrows in (b) and (c) indicate the position where a penetration depth of 1.3 mm was reached.

(g)−(i)) highlighted an obvious tissue loss in the dorsal white matter at the injury site, which is consistent with the VPA image. The tissue loss may be attributed to myelin degeneration as a result of secondary injury. In the VPA image of FA-GC treated spinal cord (Fig.8(f)), there was no abrupt VPA signal loss on the dorsal surface of the spinal cord, indicating white matter recovery after the treatment. The 3D VPA image further confirmed their findings and provided with additional information on the dimensions of the injury (Fig.8 (j) and (k)) and FA-GC treatment-mediated recovery (Fig.8(l)).

Based on VPA imaging with 1730 nm excitation, where the first overtone vibration of CH_2 bond is located, they have assessed white matter loss after a contusive SCI in adult rats. Using the first overtone vibration of CH_2 bond as the contrast, it allowed label-free mapping of white matter in an intact spinal cord and observation of physiological changes before and after injury. Moreover, the recovery of the spinal cord from contusive injury with the treatment of a neuroprotective nanomedicine, FA-GC, was also observed.

V. ASSESSING TUMOR MARGIN

The vibrational contrast mechanism has further led to the development of vibrational photoacoustic tomography (VPAT) [22, 23]. In the tomography system, a high-energy pulsed laser was applied for diffused photon excitation of the entire sample; meanwhile, an ultrasound array was used to detect the generated vibrational photoacoustic signal and reconstruct the tomographic image. Under this configuration, VPAT has been proven the imaging capability of several centimeters deep into biological tissue for imaging C−H rich biological components [22].

Using fat and hemoglobin as endogenous contrasts, Li *et al.* demonstrated a multispectral photoacosutic tomography (PAT) system to assess breast tumor mar-

DOI:10.1063/1674-0068/28/cjcp1504069

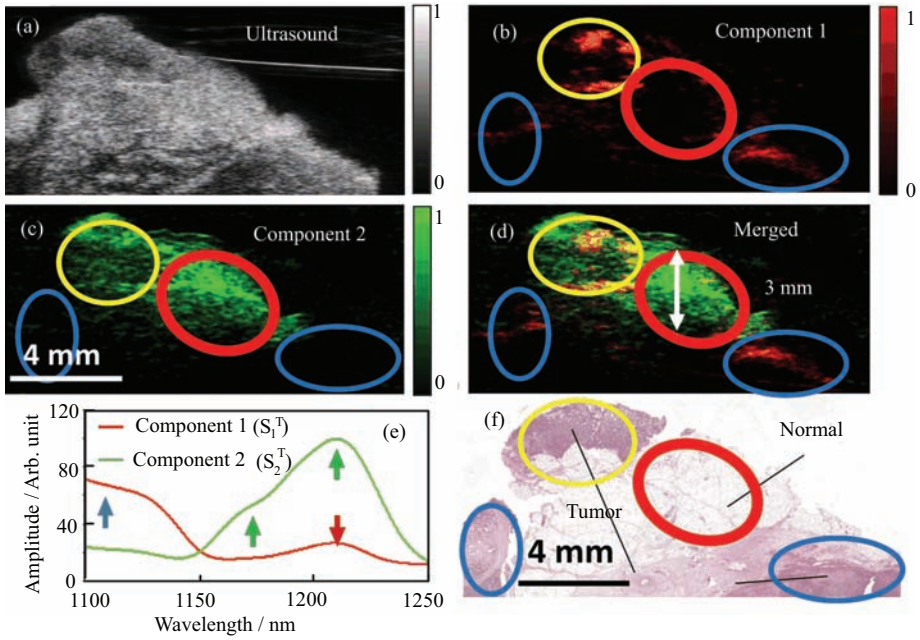

FIG. 9 Spectroscopic PA study of the excised breast tissue from human. (a) Ultrasound image, (b) image of component 1 showing the hemoglobin contrast, (c) image of component 2 showing the fat contrast, (d) the merged image indicating an imaging depth of 3 mm, (e) spectra of components 1 and 2, and (f) H&E histology image [23]. The blue arrow indicates hemoglobin absorption. The red and green arrows indicate the second overtone absorption peaks contributed by lipids.

gin [23]. Detailed experiment was performed to demonstrate the concept of differentiating cancer from normal breast tissue as shown in Fig.9. As the US image only provides the tissue morphology and the US contrast was too vague to distinguish the tumor versus the normal tissue (Fig.9(a)), a multispectral PAT with excitation ranging from 1100 nm to 1250 nm was performed. By multivariate curve resolution analysis, two chemical maps and two corresponding spectral profiles were generated, representing two major components in the tissue (Fig.9 (b)−(e)). One is mainly contributed by hemoglobin absorption (blue arrow) based on electronic absorption and the other accounts for fat based on second overtone absorption at 1210 nm (red arrow). In the meantime, up to 3 mm imaging depth was proven (Fig.9(d)). The results have been further validated by histology study. Based on the HE staining section (Fig.9(f)) of the same tissue, the area with fat and lacking hemoglobin contrast was assigned to be normal tissue with fat and scattered fibrous tissue (red oval). The area with hemoglobin and fat contrast indicated angiogenesis and invasive tumor with scattered fat tissue (yellow oval). The area without fat contrast indicated tumor tissue with dense fibrous tissue (blue oval). These results collectively demonstrated the capacity of differentiating tumor from fat or fat with fibrous tissue based on the contrast of hemoglobin and fat. The system highlights a great potential to be used clinically for intraoperative margin assessment.

VI. FUTURE PROMISE

As a label-free imaging modality with chemical selectivity and millimeter-to-centimeter-depth resolvability, vibrational photoacoustics imaging provides a new avenue to map the chemical content of biological tissue. The broad applicability of this emerging technique will be demonstrated in the years to come. It will likely benefit research and show great promise for clinical applications as well.

VII. ACKNOWLEDGMENTS

This work was supported by NIH (No.EB015901) and AHA National Innovation Award to JXC. The authors cordially thank Dr. Li-hong Wang and Dr. Michael Sturek for their collaborative effort in developing overtone vibrational transition as a new contrast mechanism for photoacoustic imaging.

[1] M. D. Morris and G. S. Mandair, *Biomedical Applications of Raman Imaging. Raman, Infrared, and Near-Infrared Chemical Imaging*, New York: John Wiley & Sons (2010).
[2] A. Zumbusch, G. R. Holtom, and X. S. Xie, Phys. Rev. Lett. **82**, 4142 (1999).

DOI:10.1063/1674-0068/28/cjcp1504069

[3] C. W. Freudiger, W. Min, B. G. Baar, S. Lu, G. R. Holtom, C. He, J. C. Tsai, J. X. Kang, and X. S. Xie, Science **322**, 1857 (2008).
[4] J. X. Cheng and X. S. Xie, *Coherent Raman Scattering Microscopy*, Boca Raton: CRC Press, (2012).
[5] A. G. Bell, Am. J. Sci. **20**, 305 (1880).
[6] L. V. Wang and S. Hu, Science **335**, 1458 (2012).
[7] J. W. Kim, E. I. Galanzha, E. V. Shashkov, H. M. Moon, and V. P. Zharov, Nat. Nanotechnol. **4**, 688 (2009).
[8] D. Razansky, M. Distel, C. Vinegoni, R. Ma, N. Perrimon, R. W. Koster, and V. Ntziachristos, Nat. Photonics **3**, 412 (2009).
[9] H. Wang, Y. Fu, and J. X. Cheng, JOSA B **24**, 544 (2007).
[10] H. W. Wang, N. Chai, P. Wang, S. Hu, W. Dou, D. Umulis, L. V. Wang, M. Sturek, R. Lucht, and J. X. Cheng, Phys. Rev. Lett. **106**, 238106 (2011).
[11] H. W. Siesler, Y. Ozaki, S. Kawata, and H. M. Heise, *Near-Infrared Spectroscopy: Principles, Instruments, Applications*, New York: John Wiley & Sons, (2008).
[12] P. Wang, H. W. Wang, M. Sturek, and J. X. Cheng, J. Biophotonics **5**, 25 (2012).
[13] T. J. Allen, A. Hall, A. P. Dhillon, J. S. Owen, and P. C. Beard, J. Biomed. Opt. **17**, 0612091 (2012).
[14] K. Jansen, M. Wu, A. F. W. van der Steen, and G. van Soest, Photoacoustics **2**, 12 (2014).
[15] X. Li, W. Wei, Q. Zhou, K. K. Shung, and Z. Chen, J. Biomed. Opt. **17**, 106005 (2012).
[16] K. Jansen, A. F. W. van der Steen, H. M. M. van Beusekom, J. W. Oosterhuis, and G. van Soest, Opt. Lett. **36**, 597 (2011).
[17] B. Wang, A. Karpiouk, D. Yeager, J. Amirian, S. Litovsky, R. Smalling, and S. Emelianov, Opt. Lett. **37**, 1244 (2012).
[18] P. Wang, T. Ma, M. N. Slipchenko, S. Liang, J. Hui, K. K. Shung, S. Roy, M. Sturek, Q. Zhou, Z. Chen, and J. X. Cheng, Sci. Rep. **4**, 6889 (2014).
[19] X. Bai, X. Gong, W. Hau, R. Lin, J. Zheng, C. Liu, C. Zeng, X. Zou, H. Zheng, and L. Song, PLOS ONE **9**, 92463 (2014).
[20] J. Zhang, S. Yang, X. Ji, Q. Zhou, and D. Xing, J. Am. Coll. Cardiol. **64**, 385 (2014).
[21] W. Wu, P. Wang, J. X. Cheng, and X. M. Xu, J. Neurotrauma **31**, 1998 (2014).
[22] J. R. Rajian, R. Li, P. Wang, and J. X. Cheng, J. Phys. Chem. Lett. **4**, 3211 (2013).
[23] R. Li, P. Wang, L. Lan, F. P. Lloyd, C. J. Goergen, S. Chen, and J. X. Cheng, Biomed. Opt. Express **6**, 1273 (2015).

DOI:10.1063/1674-0068/28/cjcp1504069